Electron-wave-packet-deformation–induced attosecond emission time shift in gas high-order harmonic generation

Sen Qiao,[1] Liang Li [●],[1,*] Pengfei Lan,[1,†] and Peixiang Lu [●][1,2,3]

[1]*Wuhan National Laboratory for Optoelectronics and School of Physics,*
Huazhong University of Science and Technology, Wuhan 430074, China
[2]*Hubei Key Laboratory of Optical Information and Pattern Recognition, Wuhan Institute of Technology, Wuhan 430205, China*
[3]*CAS Center for Excellence in Ultra-Intense Laser Science, Shanghai 201800, China*

The laser-induced recollision of electron trajectories is usually used to describe high-order harmonic generation (HHG), which also lays the foundation for high-order harmonic spectroscopy. Electron trajectory models based on the saddle-point approximation are conceptually similar to the light ray model in optics. Considering that ray optics is not complete to explain all wave optics phenomena, we revisit the validity of trajectory models when incorporating the Coulomb potential. Results show that, under commonly used gas HHG experimental conditions, both the classical three-step model and the quantum orbit model have dozens or hundreds of attoseconds of deviation in emission time. By using the Gaussian wave-packet method, we reveal that the time shift can be attributed to the deformation of the recollision electron wave packet. Wave-packet deformation is an inherent wavelike phenomenon caused by group delay dispersion and higher-order dispersion, and thereby is difficult to modify by particlelike trajectories. In addition, we reveal the notable influence of wave-packet deformation on observables in two-color field HHG experiments.

I. INTRODUCTION

High-order harmonic generation (HHG) is an extremely nonlinear and nonperturbative optical up-conversion process that occurs when an intense laser interacts with matter. Its physical picture is usually explained in terms of the laser-induced recollision of electron trajectories [1]. Due to its unique time-frequency features, HHG can be utilized as coherent light sources in extreme ultraviolet and x-ray regions [2–5], and to generate attosecond pulses [6,7]. Additionally, the recollision process can be seen as a self-probe of the electron wave function. The analysis of the HHG signal enables the extraction of both static [8–10] and dynamical [11–14] information of electrons with both angstrom spatial resolution and attosecond temporal resolution [15], which is known as high-order harmonic spectroscopy (HHS) [16,17].

The trajectory-resolved model is the foundation of HHS. The interference of trajectories links the electron dynamics with experimental observables, and thereby enables the retrieval of ionization and recombination time [18–20] and the transition dipole moment [17,21]. The accurate modeling of electron trajectories is pivotal for HHS applications. In the well-known classical three-step model [1], electrons are first ionized and subsequently accelerated by laser fields. The trajectories are given by classical Newtonian motion equations. High-order harmonics are generated when trajectories return to the core. This classical model (CM) interprets the plateau

and cutoff structure of harmonic spectra in a straightforward and intuitive way. The quantum-mechanical version of the three-step model is known as the strong-field approximation (SFA) model [22,23]. It provides a more sophisticated path-integral formulation for quantitatively calculating the HHG spectrum. By performing the saddle-point approximation (SPA), the SFA model yields complex-valued electron trajectories, which are known as quantum orbits (QOs) [24].

In the original formulation of the CM and SFA, the Coulomb interaction between the electron and core is neglected when the electron propagates in the continuum. However, both the retrieved results from HHS experiments [17–19] and the theoretical results acquired by numerically solving the time-dependent Schrödinger equation (TDSE) [25–27] demonstrate that the Coulomb potential can induce time shifts in ionization and recombination. The time shifts range from dozens to hundreds of attoseconds, which has non-negligible influence on applications of HHS. Aiming to modify the Coulomb interaction, various improved models have been proposed [28]. In the classical trajectory Monte Carlo (CTMC) [29] and Coulomb-modified SFA [30] methods, Coulomb force is incorporated into Newtonian equations. Additionally, in the quantum trajectory Monte Carlo [31] and analytical R-matrix (ARM) [32–34] methods, an additional phase term involving the Coulomb potential is attached.

According to Feynman's path integral, HHG can be represented as a coherent superposition of contributions from all possible paths [24]. The trajectory-resolved models are based on the saddle-point approximation. The SPA reduces the infinite path integral into a few classical trajectories or quantum orbits. Generally, previous Coulomb-corrected models make

*liangl@hust.edu.cn
†pengfeilan@hust.edu.cn

modifications within the framework of SPA. They either calculate Coulomb-corrected classical trajectories or modify the phase and derive modified quantum orbits. Basically, they still relate the generation of given harmonics with a certain trajectory. The SPA is conceptually similar to Fermat's principle, and the electron trajectories correspond to light rays. Just as not all wave optics phenomena can be well explained by ray optics, the trajectory models are simplified models that are not complete for describing all wavelike phenomena. Recently, the Huygens-Fresnel picture of solid HHG has been proposed [35,36]. Instead of using recollision trajectories, it uses the perspective of wavelet interference to model the generation of solid high-order harmonics. It has been demonstrated that particlelike trajectories are insufficient to trace electron wave-packet deformation induced by the nonparabolic dispersion of a solid energy band. In gas HHG, the Coulomb potential can also make the continuum electron wave packet deformed, which makes the validity of SPA questionable.

In this paper, we investigate the Coulomb-induced emission time shift in gas HHG. We reveal the important role of wave-packet deformation and discuss the limitations of SPA. This paper is organized as follows. In Sec. II, we introduce the theoretical approaches. We introduce the extraction method of emission time from TDSE calculations. Next, we make a brief review of the commonly used trajectory models. Using the comparison between geometric optics and wave optics as an analogy, we discuss the foundation of SPA and trajectory models. Then we introduce the Gaussian wave-packet method (GWM). In Sec. III, we present our main results and discussions. Our results show notable disagreement between commonly used models and full quantum TDSE simulations. We demonstrate that the wave-packet deformation is responsible for the deviation. Additionally, in order to study the influence of deformation on HHS, we investigate the results of two-color field experiments. We show that, via interference, the wave-packet deformation can have a notable influence on experimental observables. Finally, we conclude in Sec. IV.

II. THEORETICAL APPROACHES

A. TDSE calculation

In length gauge, the time-dependent Schrödinger equation is given by

$$
\frac{\partial}{\partial t}\psi(\mathbf{r}, t) = \hat{H}\psi(\mathbf{r}, t)
$$
$$
= \left[-\frac{1}{2}\overset{2}{\nabla} + V(\mathbf{r}) + \mathbf{r} \cdot \mathbf{E}(t)\right]\psi(\mathbf{r}, t). \quad (1)
$$

Atomic units (a.u.) are used throughout this paper unless stated otherwise. $\psi(\mathbf{r}, t)$ is the time-dependent wave function of the system. $\hat{H}$ denotes the Hamiltonian. We consider a Coulomb potential of a hydrogen atom in the form of $V(\mathbf{r}) = -Ze^{-\rho r^2}/\sqrt{r^2 + \xi}$. ρ is the screening parameter with $\rho = 0$ for the long-range potential and $\rho > 0$ for the short-range potential [37]. ξ is the smoothing parameter, and Z is the effective charge. Unless stated otherwise, $Z = 0.9495$, $\rho = 0$, and $\xi = 0.5$ are used to match the ionization potential $I_p = 0.5$ a.u. of the hydrogen atom. The initial ground state ψ_0 is prepared by imaginary-time propagation [38]. A linearly

polarized driving field $\mathbf{E}(t) = f(t)E_0 \cos(\omega t)\hat{\mathbf{e}}_x$ is applied to this atom. $f(t)$ is a trapezoidal envelope with a one-cycle rising and falling edge and one-cycle plateau. The time-dependent evolution of the wave function is obtained by numerically solving Eq. (1) through the split-operator method [39]. At each time step, the wave function is multiplied with an absorbing mask function $M(r)$ to eliminate the spurious reflection from the boundary:

$$
M(r) = \begin{cases} 1 & r \leqslant R \\ \cos^{1/8}\left[\frac{\pi(r-R)}{2L}\right] & R < r \leqslant R + L \\ 0 & r > R + L \end{cases} \quad (2)
$$

Here $L = 25$ a.u. denotes the width of the absorbing area. In our simulation, the space step is $dx = dy = 0.2$ a.u., and the time step is $dt = 0.05$ a.u. Once the time-dependent wave function $\psi(\mathbf{r}, t)$ is calculated, the induced dipole acceleration $\mathbf{a}(t)$ is calculated via the Ehrenfest theorem, and the high-order harmonics $\mathbf{D}(\Omega)$ can be obtained by Fourier transformation:

$$
\mathbf{a}(t) = \langle\psi(\mathbf{r}, t)| - \nabla V(\mathbf{r}) - \mathbf{E}(t)|\psi(\mathbf{r}, t)\rangle,
$$
$$
\mathbf{D}(\Omega) \propto \int \mathbf{a}(t)e^{-i\Omega t}dt. \quad (3)
$$

To extract the time-frequency property of HHG, we resort to the Gabor analysis [40]:

$$
I_G(\Omega, t) = \sum_{j=x,y}\left|\int a_j(t')e^{-(t-t')^2/2\tau^2 - i\Omega t'}dt'\right|^2. \quad (4)
$$

There are short, long, and multiple recombination trajectories that contribute to the generation of the same harmonics [41,42]. Experimentally, each channel can be selected by controlling phase matching [43]. Since the envelope of the laser that we use just has a one-cycle plateau, the multiple recombination signal can be neglected. The short and long trajectory signals can be selected by adjusting the absorbing mask $M(r)$. According to CM, the maximal displacement of short trajectories is about $1.127x_m$, where $x_m = E_0/\omega^2$, and that in long trajectories is about $2x_m$. Therefore, the short trajectory harmonics $\mathbf{D}_s$ can be selected by setting $R = 1.127x_m$ [44,45]. The superposition of short and long harmonics $\mathbf{D}_{s+l}$ can be calculated by setting $R = 2x_m$. Then the long trajectory harmonics can be obtained as $\mathbf{D}_l = \mathbf{D}_{s+l} - \mathbf{D}_s$. It should be noted that the separating is difficult in the cutoff region where the short and long trajectories mutually merge. Therefore, we pay more attention to the plateau HHG. Figure 1 shows the separated signal of short and long trajectory HHG. Here we first extract short and long trajectory signals and draw their Gabor time-frequency distributions individually. Then we overlay these two figures together. For given harmonic frequency Ω, the temporal position t_r of local maxima of $I_G(\Omega, t)$ is regarded as the emission time. The solid blue and orange lines show the extracted emission time of short and long trajectory HHG respectively. The ionization time t_i, which is difficult to extract directly, is less discussed in this paper.
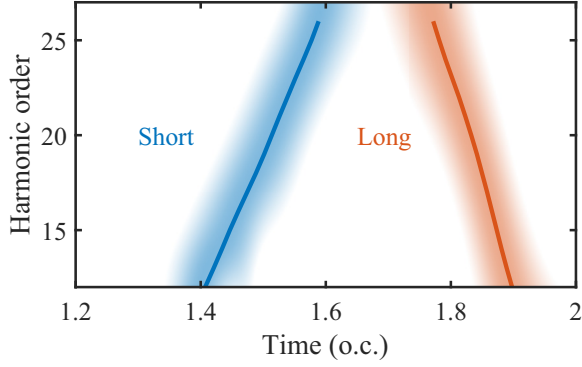
FIG. 1. Gabor time-frequency distribution of harmonic emission. The short and long trajectory HHG profiles are extracted respectively and then overlaid together. The wavelength of laser is 800 nm and the intensity is $0.15\,\mathrm{PW/cm^2}$. The blue (left) and orange (right) solid lines denote the emission time of short and long trajectory harmonics when intensity reaches local maxima.

B. Trajectory-resolved models

In the classical three-step model, the initial longitudinal velocity of electrons is assumed to be zero. After ionization, electrons are accelerated by the laser field:

$$
\begin{aligned}
\mathbf{v}(t_i) \cdot \mathbf{E}(t_i) &= \mathbf{0}, \\
\mathbf{v}(t) &= \mathbf{v}(t_i) - \mathbf{A}(t_i) + \mathbf{A}(t), \\
\int_{t_i}^{t_r} \mathbf{v}(\tau)d\tau &= \mathbf{0}, \\
v(t_r)^2/2 + I_p &= \Omega.
\end{aligned} \tag{5}
$$

Here $\mathbf{A}(t) = -\int \mathbf{E}(t)dt$ is the vector potential of the driving field. High-order harmonics are generated when electrons recollide with the parent ion. The mapping between harmonic frequency Ω and return time t_r is built via the conservation law of energy at t_r.

The SFA model gives a quantum-mechanical counterpart of the three-step model. The high-order harmonics $\mathbf{D}(\Omega)$ are contributed by trajectories with different ionization time t_i, recombination time t_r, and canonical momentum $\mathbf{p}$:

$$
\begin{aligned}
\mathbf{D}(\Omega) &\propto \int dt_i \int dt_r \int d\mathbf{p} \, \mathbf{W}(t_i, t_r, \mathbf{p})e^{-iS(t_i, t_r, \mathbf{p})}, \\
\mathbf{W}(t_i, t_r, \mathbf{p}) &= \mathbf{d}^*[\mathbf{p} + \mathbf{A}(t_r)]\mathbf{E}(t_i)\mathbf{d}[\mathbf{p} + \mathbf{A}(t_i)], \\
S(t_i, t_r, \mathbf{p}) &= \int_{t_i}^{t_r} \{[\mathbf{p} + \mathbf{A}(\tau)]^2/2 + I_p\}d\tau - \Omega t_r.
\end{aligned} \tag{6}
$$

Here W and S are the weight and phase factors of trajectories. For atomic gas, the dipole matrix element $\mathbf{d}(\mathbf{k})$ changes smoothly over tens of electron volts. The S varies on a characteristic scale $\approx 1/(t_r - t_i)$. Since $t_r - t_i$ can be approximated as half of the optical cycle (o.c.) of the driving laser, the S varies thus much faster than the other factors [22,23]. Therefore, the e^{-iS} in the integrand yields a very strong oscillation. Consequently, the integral of $\mathbf{D}(\Omega)$ accumulates predominantly near the saddle points where S is stationary, which is known as the saddle-point approximation [24,36,46]. The SPA allows one to reduce the integral into a few quantum orbits [23,47]. By

solving the following saddle equations, the ionization time, recombination time, and canonical momentum of the QO can be calculated:

$$
\begin{aligned}
\frac{\partial S}{\partial t_i} &= \frac{1}{2}[\mathbf{p} + \mathbf{A}(t_i)]^2 + I_p = 0, \\
\frac{\partial S}{\partial t_r} &= \frac{1}{2}[\mathbf{p} + \mathbf{A}(t_r)]^2 + I_p - \Omega = 0, \\
\frac{\partial S}{\partial \mathbf{p}} &= \int_{t_i}^{t_r}[\mathbf{p} + \mathbf{A}(\tau)]d\tau = 0.
\end{aligned} \tag{7}
$$

As introduced in [26,32], the QO can be corrected to the first order in the electron-core interaction by ARM theory, in which a Coulomb term S_c is added to the SFA phase:

$$
S_c = \int_{t_k}^{t_{\mathrm{end}}} V[\mathbf{r}_a(\tau)]d\tau. \tag{8}
$$

Here $\mathbf{r}_a(t)$ is the potential-free trajectory. The lower limit of the integral in Eq. (8) is determined by a boundary-matching procedure which leads to $t_k = t_i - i/(2I_p)$. The upper limit is found by the condition $\sqrt{\mathbf{r}_a^2(t_{\mathrm{end}})} = r_0$, where $r_0 = \frac{1}{2v_r}e^{2\{0.5772 - \sum_{p=1}^{\infty}[1 - v_r p \, \mathrm{arccot}(v_r p)]/p\}}$ [48]. The Coulomb phase term leads to the shifts of the real parts of the saddle-point times (for more details, see Appendix A in [32]):

$$
\begin{aligned}
\delta t_i &= -\frac{\partial \mathrm{Re}(S_c)}{\partial I_p} - \frac{\partial \mathrm{Re}(S_c)}{\partial \Omega}, \\
\delta t_r &= -\frac{\partial \mathrm{Re}(S_c)}{\partial \Omega}.
\end{aligned} \tag{9}
$$

The analog of SPA in optics is Fermat's principle, and electron trajectories correspond to light rays. In contrast, Huygens-Fresnel's principle provides a more comprehensive wave picture. Here we use the comparison between geometric optics and wave optics as an analogy to discuss the validity of SPA in gas HHG. Figures 2(a1)–2(a3) illustrate the propagation of light beams in three different kinds of medium. The black dashed lines denote the wavefronts. The blue lines denote the light rays that are perpendicular to the wavefronts. The orange arcs denote the secondary wavelets emanating from each point on the wavefronts. According to Huygens-Fresnel's principle, the superposition of wavelets forms a new wavefront. Figure 2(a1) depicts the simplest case. A beam of light travels through a homogeneous medium. One can use a straight light ray to describe the propagation. Figure 2(a2) shows the propagation in an inhomogeneous medium where the refractive index changes linearly in space. The lower area has a larger refractive index. The wavefronts tilt gradually but remain in plane. The normals at each point on the same wavefront remain mutually parallel. Therefore, one can still use a bending ray to describe the propagation. Figure 2(a3) shows a more complicated case, where the refractive index has high-order nonlinear distribution in space. The inhomogeneity consists of Gaussian distributions besides the linear term. The wavefronts are deformed and the normals are no longer parallel to each other. It is insufficient to use only one light ray to describe the propagation, while Huygens-Fresnel's principle is of more validity.

In gas HHG, the SPA has been proven to be valid when completely neglecting the Coulomb potential [46]. It corre-
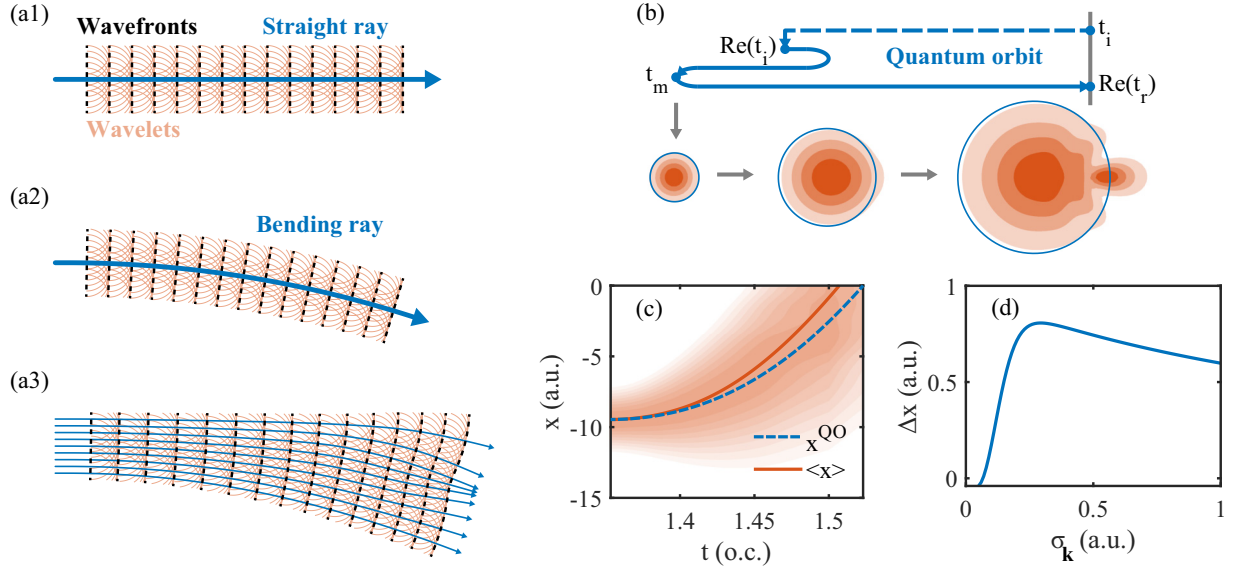
FIG. 2. (a1–a3) The propagation of light beams in different kinds of media. (a1) The propagation in a homogeneous medium. (a2) The propagation in an inhomogeneous medium where the refractive index changes linearly in space. (a3) The propagation in an inhomogeneous medium where the refractive index changes nonlinearly in space. (b) Schematic illustration of the quantum orbit and Gaussian wave-packet method. (c) The pseudocolor shows the profile of the time-dependent wave packet. The orange solid line shows the effective trajectory of the wave packet. The blue dashed line shows the QO result. (d) The defined degree of wave-packet deformation with initial width changing. In (c) and (d), the wavelength of the laser is 800 nm and the intensity is 0.15 PW/cm^2. The results correspond to the electron trajectory of H19.

sponds to the case shown in Fig. 2(a1). HHG can be well described in terms of free electron trajectories. The problem is how to account for the effect of the Coulomb potential. Previous works, like ARM, correct the Coulomb effect within the framework of SPA. It is similar to the case shown in Fig. 2(a2). The correction is valid provided the Coulomb effect is perturbative and does not influence the foundation of SPA. In SPA, the reduction for the path integral consists of two steps. In the first step, the entire integral is reduced into the integral over the vicinity of saddle points at which the first partial derivative of $S(t_i, t_r, \mathbf{p})$ equals zero. In the second step, the $S(t_i, t_r, \mathbf{p})$ is approximated as a truncated Taylor expansion up to the second order in the vicinity of saddle points [23]. Hence the integral over the vicinity can be approximated as a Gaussian integral. Clearly, the second reduction is based on the assumption that in the Taylor expansion the second-order term dominates over higher-order terms [36]. In a local space, the Coulomb potential can be seen as an influence on the dispersion of free electrons. The $S(t_i, t_r, \mathbf{p})$ cannot be simply treated as a quadratic function of $\mathbf{p}$. Similar to the case in solid HHG [35], the group delay dispersion and higher-order dispersion can lead to the wave-packet deformation, which makes the validity of SPA questionable.

C. Gaussian wave-packet method

In this section, we introduce the Gaussian wave-packet method. A general propagator $\hat{K}(t, t_0)$, describing the propagation of the wave function from t_0 to t, satisfies fundamental properties as

$$|\psi(t)\rangle = \hat{K}(t, t_0)|\psi(t_0)\rangle,$$
$$\hat{K}(t, t_0) = \hat{K}(t, t_m)\hat{K}(t_m, t_0). \tag{10}$$

Here the t_m denotes an arbitrary middle time. Using Eq. (10) and inserting a Gaussian projection operator, the wave function $\psi(\mathbf{r}, t)$ in Eq. (3) can be rewritten as

$$\psi(\mathbf{r}, t) = \langle \mathbf{r}|\psi(t)\rangle$$
$$= \iint \langle \mathbf{r}|\hat{K}(t, t_m)|\psi_G, \mathbf{r}_c, \mathbf{k}_c, \sigma_{\mathbf{k}}\rangle$$
$$\times \langle \psi_G, \mathbf{r}_c, \mathbf{k}_c, \sigma_{\mathbf{k}}|\hat{K}(t_m, t_0)|\psi(t_0)\rangle d\mathbf{r}_c d\mathbf{k}_c. \tag{11}$$

Here the set of Gaussian wave packets $|\psi_G, \mathbf{r}_c, \mathbf{k}_c, \sigma_{\mathbf{k}}\rangle$ forms an overcomplete basis [49]:

$$\langle \mathbf{r}|\psi_G, \mathbf{r}_c, \mathbf{k}_c, \sigma_{\mathbf{k}}\rangle = \sqrt{\frac{\sigma_{k_x}\sigma_{k_x}}{\pi}} \exp\left[-\frac{\sigma_{k_x}^2(x - x_c)^2}{2}\right.$$
$$\left. - \frac{\sigma_{k_y}^2(y - y_c)^2}{2} + i(k_{x_c}x + k_{y_c}y)\right]. \tag{12}$$

(x_c, y_c), (k_{x_c}, k_{y_c}), and $(\sigma_{k_x}, \sigma_{k_y})$ represent the central position, central momentum, and standard deviation of momentum. The physical picture behind Eq. (11) is similar to Huygens-Fresnel's principle shown in Figs. 2(a1)–2(a3). At t_m, the wave function can be expressed as a superposition of Gaussian wave packets. The wave packets serve as secondary sources, propagating and mutually interfering. The HHG is contributed by all wave packets. It should be noted that because of the overcompleteness of Gaussian wave packets Eq. (11) as it stands is not exact. Since our goal is to qualitatively investigate the influence of wave-packet deformation on SPA, we can make further reductions. As Fig. 2(b) shows, for HHG with given energy, we first select the most representative Gaussian wave packets based on QO results,

and then trace the wave-packet deformation. Here the dashed blue line denotes the tunneling process occurring during complex-valued time from $\text{Re}(t_i) + \text{Im}(t_i)$ to $\text{Re}(t_i)$. The tunneling is a quantum-mechanical process with no classical counterpart. After tunneling, the QO is conceptually related to the classical three-step model. The movement follows classical Newtonian equations. The solid blue line shows the trajectory during real-valued time from $\text{Re}(t_i)$ to $\text{Re}(t_r)$. We regard the time when the electron drifts farthest from the parent ion as t_m:

$$\mathbf{k}^{\text{QO}}(t_m) = \text{Re}[\mathbf{p} + \mathbf{A}(t_m)] = \mathbf{0},$$

$$\mathbf{r}^{\text{QO}}(t_m) = \text{Re}\left\{ \int_{t_i}^{t_m} [\mathbf{p} + \mathbf{A}(\tau)]d\tau \right\}. \qquad (13)$$

At this time, we release an initial Gaussian wave packet, the central position and momentum of which are consistent with QO results. It corresponds to performing an approximation that reduces the $\langle \psi_G, \mathbf{r}_c, \mathbf{k}_c, \sigma_{\mathbf{k}} | \hat{K}(t_m, t_0) | \psi(t_0) \rangle$ into $\delta[\mathbf{r}_c - \mathbf{r}^{\text{QO}}(t_m)]\delta[\mathbf{k}_c - \mathbf{k}^{\text{QO}}(t_m)]$. Here the δ symbolizes the Dirac delta function. Therefore, the integral in Eq. (11) becomes $\langle \mathbf{r} | \hat{K}(t, t_m) | \psi_G, \mathbf{r}^{\text{QO}}(t_m), \mathbf{k}^{\text{QO}}(t_m), \sigma_{\mathbf{k}} \rangle$. The above reduction means that the SPA makes a prefiltering for the Gaussian wave packets at t_m. The contribution from those wave packets that deviate far from saddle points is neglected. The reason for choosing the Gaussian expansion at the maximal excursion time is that the Coulomb effect is relatively weak in the far field, which facilitates the simplification. By contrast, at ionization time, electrons are too close to the parent ion. As a result, the electron wave packet receives strong Coulomb interaction, and can split into several separated wave packets. It forces us to trace the propagation of more than one wave packet which makes the analysis complicated and not intuitive. It should be noted that since we make the reduction based on QO results the Coulomb effect before t_m is not well incorporated. It may introduce certain deviations for quantitative results. But here we focus on the physical picture rather than accurate calculation. The approximations do not impact our main conclusions. After t_m, the time-evolution operator $\hat{K}(t, t_m)$ is carried out by solving the TDSE. Our simulation differs from previous field-free Gaussian wave-packet collision methods [50,51] in the following aspects.

(1) The momentum width of the wave packet is not quite narrow.

(2) The initial central position is not far enough from the ionic core.

(3) The laser field acts on the wave packet during propagation.

(4) The ground state is unoccupied initially.

The bottom of Fig. 2(b) illustrates the initial wave packet and the subsequent deformed wave packet. For a clear comparison, we attach blue circles to show the outline of the wave packet in Coulomb-free propagation. In the absence of potential, the dispersion of the free electron is parabolic. The wave packet spreads due to the group velocity dispersion, but keeps a Gaussian distribution. The full width at half maximum (FWHM) of the wave packet at a later moment t is given by [52]

$$\text{FWHM} = 2\sqrt{2\ln 2}/\sqrt{1/\sigma_{\mathbf{k}}^2 + (t - t_m)^2\sigma_{\mathbf{k}}^2}. \qquad (14)$$

In the QO model, the spreading of the wave packet is related to the weight of trajectories. In the presence of potential, the dispersion is nonparabolic. The group delay dispersion and higher-order dispersion lead to the wave-packet deformation. Like the case shown in Fig. 2(a3), it is insufficient to use particlelike trajectories to trace the wave-packet deformation. We use the average position $\langle \mathbf{r} \rangle$ and momentum $\langle \mathbf{k} \rangle$ as the effective position and momentum. The time t_r' when $\langle \mathbf{r}(t_r') \rangle = \mathbf{0}$ is recorded as the corrected recollision time and the time-energy mapping is modified by $\Omega' = \langle k(t_r') \rangle^2/2 + I_p$. In Fig. 2(c), the pseudocolor figure shows the profile of the time-dependent distribution $|\psi_G(x, y = 0, t)|^2$. At each moment, the distribution is normalized individually. Here $\sigma_{k_x} = \sigma_{k_y} = 0.5$ a.u. is used. The orange line denotes the effective displacement, and the blue dashed line denotes the uncorrected QO result. The laser wavelength is 800 nm and the intensity is 0.15 PW/cm^2. The trajectory corresponds to the 19th-order harmonics. It shows that the effective trajectory approaches the core faster than QO due to wave-packet deformation, which results in an earlier recollision with higher kinetic energy. We use the average deviation between QO and effective trajectory to define the degree of deformation:

$$\Delta x = \frac{1}{t_r' - t_m} \int_{t_m}^{t_r'} |\langle x(\tau) \rangle - x^{\text{QO}}(\tau)|d\tau. \qquad (15)$$

Next, we discuss the value setting of the factor $\sigma_{\mathbf{k}}$. Physically, $\sigma_{\mathbf{k}}$ indicates the momentum width of the continuum electron that contributes to the given HHG. Considering the uncertainty principle, its value should be neither too small nor too large. Here we set $\sigma_{\mathbf{k}}$ empirically. As introduced in previous works, the FWHM of the continuum wave packet at recombination time t_r is typically ≈ 20 Å [53]. The time interval $(t_r - t_m)$ can be approximated as a quarter of the optical cycle of the driving laser. Assuming the wavelength of the laser ranges from 800 to 1200 nm and substituting the above estimated values into Eq. (14), we can calculate the factor $\sigma_{\mathbf{k}}$ is about 0.4–0.6 a.u. We also show the dependence of Δx on $\sigma_{\mathbf{k}}$ in Fig. 2(d). When $\sigma_{\mathbf{k}}$ tends to zero, the momentum width is narrow. The Coulomb influence on dispersion can be approximated as a truncated Taylor expansion up to the low orders in the vicinity of central momentum $\mathbf{k}_c$. Therefore, the deformation effect is not obvious. As the $\sigma_{\mathbf{k}}$ increases, higher-order dispersion becomes non-negligible, and thereby the deformation effect becomes obvious. Results show that the degree of deformation gradually converges when $\sigma_{\mathbf{k}} > 0.3$ a.u.. We have verified the case for different parameters and find that the results are similar. Based on the above results, we adopt $\sigma_{\mathbf{k}} = 0.5$ a.u. in the following discussion.

III. RESULTS AND DISCUSSIONS

We commence the study with the emission time shift in short trajectory HHG. In Fig. 3(a), the gray lines show the temporal distribution $I_G(\Omega, t)$ calculated by Eq. (4). Each line is normalized individually. The black dashed lines show the extracted emission time. The laser intensity is 0.3 PW/cm^2 and the wavelength is 1000 nm. The Keldysh parameter $\gamma = \sqrt{I_p/(2U_p)}$ is 0.49, where $U_p = E_0^2/4\omega^2$ is the ponderomotive kinetic energy. We first focus on the deviation of the classical three-step model. As the blue dashed line shows, the emission
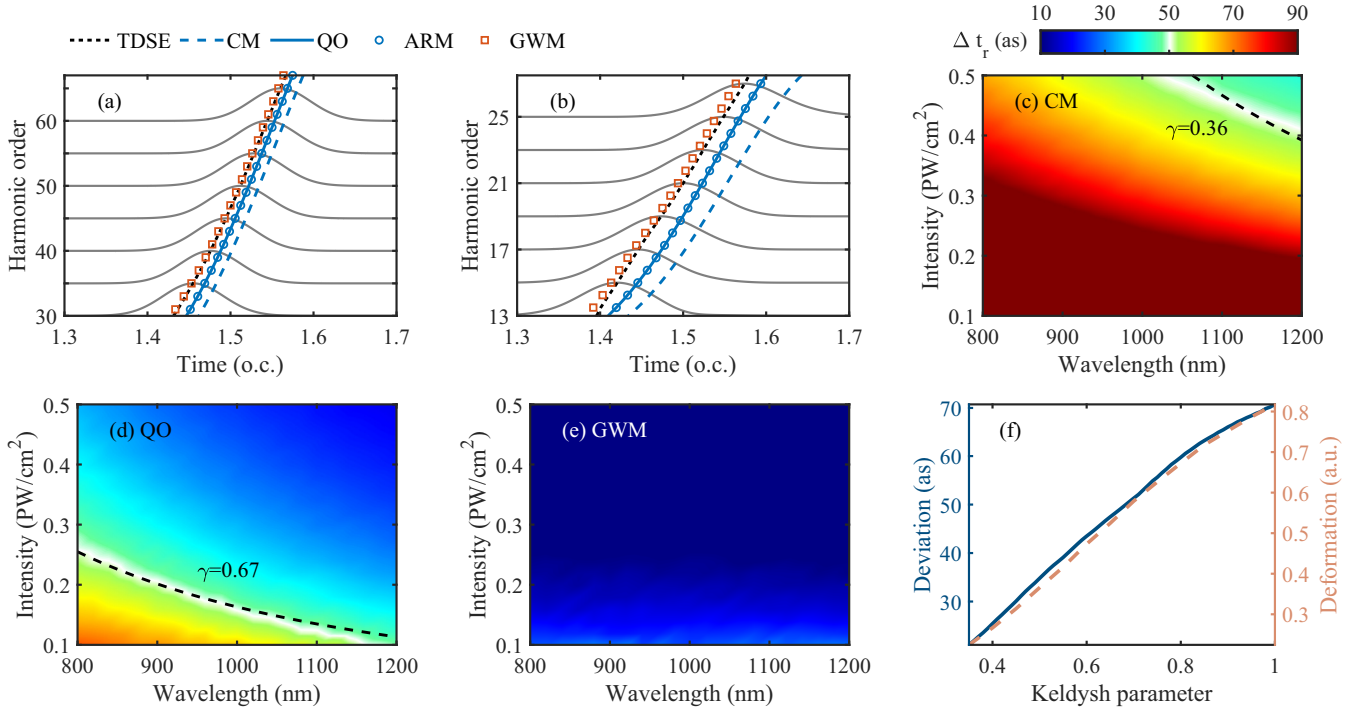
FIG. 3. (a), (b) The emission time of short trajectory harmonics. The gray lines show the temporal distribution $I_G(\Omega, t)$ of each harmonic. Each line is normalized individually. The laser in (a) has a wavelength of 1000 nm and an intensity of 0.3 PW/cm². The laser in (b) has a wavelength of 800 nm and an intensity of 0.15 PW/cm². (c)–(e) The average time shift of CM, QO, and GWM. (f) The average results of QO deviation and the degree of deformation.

time given by the CM is later than the TDSE result. It is notable that the time shift exists in the entire plateau region and hardly diminishes with the increase of harmonic order. The average time deviation Δt_r is about 0.023 o.c., corresponding to 77 as. Figure 3(b) shows the result when using lower laser intensity and shorter laser wavelength. The laser intensity is 0.15 PW/cm², and the wavelength is 800 nm. The Keldysh parameter γ equals 0.87. In this case, the discrepancy between CM and TDSE is more obvious. The average deviation reaches 145 as. Figure 3(c) shows the dependence of Δt_r on laser parameters. It is clear that the deviation increases as intensity decreases and wavelength decreases. We choose $\Delta t_r = 50$ as a threshold and highlight the contour line by adjusting the color map. The black dashed line shows the contour line of the Keldysh parameter $\gamma = 0.36$. It shows that Δt_r is related to γ. Then we move our focus to the QO results. As blue solid lines show, the time shift in QO is about half of that in the CM. In Fig. 3(a), its average deviation is 35 as, and in Fig. 3(b) the average deviation is 65 as. As Fig. 3(d) shows, in the QO model, the contour line of $\Delta t_r = 50$ as corresponds to $\gamma = 0.67$. Next, we compare the correction given by ARM and Gaussian wave-packet method (GWM). As reported in previous researches [26,32], ARM can obviously reduce the ionization time shift, but the correction for emission time is less obvious. As blue circles in Figs. 3(a) and 3(b) show, the ARM results are almost the same as the QO ones. We have verified the results under different laser parameters and find that ARM always gives nearly identical emission time with QO. As orange squares show, the GWM gives earlier emission time than the QO model. It is seen that

GWM results correspond well with TDSE results. As Fig. 3(e) shows, the time shift can be well eliminated by GWM under different laser parameters. We average results from different laser wavelengths but the same γ. As Fig. 3(f) shows, both Δt_r and Δx increase almost linearly with γ. It should be noted that in gas HHG experiments the driving laser with 800 nm of wavelength is commonly used, and γ usually approximately equals 1. In this parameter region, CM, QO, and ARM exhibit deviation of dozens or hundreds of attoseconds, which has non-negligible influence on the applications of HHS that has attosecond precision.

Next, we investigate the role of the Coulomb potential. First, we calculate the TDSE with a short-range potential. Here $Z = 1.77$, $\rho = 1$, and $\xi = 0.5$ are used, and the laser parameters are the same as those in Fig. 3(b). As shown in Fig. 4(a), in this case, the TDSE results are nearly identical with QO results. The average deviation is merely 7 as. It indicates that the deviation of QO mainly stems from the long-range Coulomb effect. We divide the total potential into short-range and long-range parts as follows:

$$V(\mathbf{r}) = \beta V^S + (1 - \beta)V^L = \frac{\beta Z^S e^{-\rho r^2} + (1 - \beta)Z^L}{\sqrt{r^2 + \xi}}. \quad (16)$$

The smoothing parameter ξ is fixed at 0.5 and the effective charges Z^S and Z^L are adjusted to keep the ionization potential constant. The β and ρ determine the depth and width of the long-range Coulomb tail. As illustrated in Figs. 4(b) and 4(c), the time shift Δt_r and wave-packet deformation Δx have similar variation. The larger proportion of the long-range tail leads
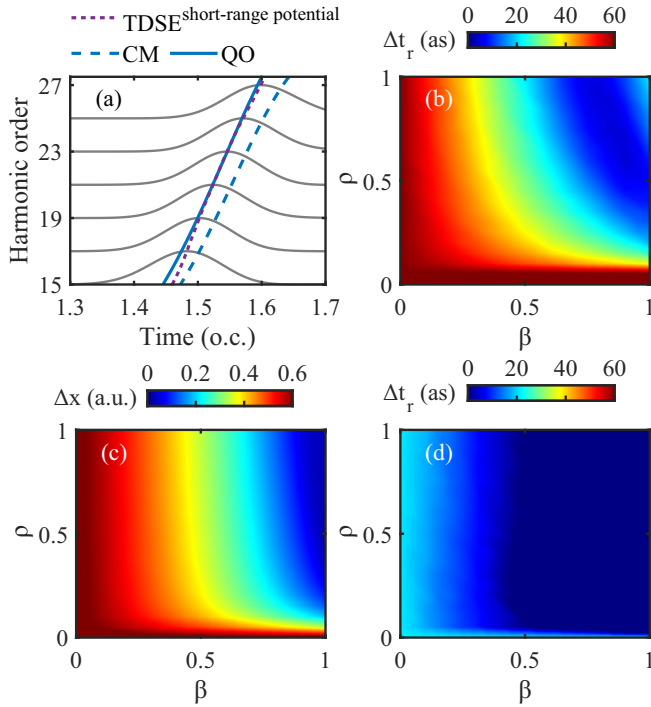
FIG. 4. (a) The emission time of short trajectory harmonics. The laser parameter is the same as that in Fig. 3(b), but a short-range potential is used in TDSE calculation. (b) The emission time shift in the QO model. (c) The degree of wave-packet deformation calculated by GWM. (d) The emission time shift in GWM.

to the larger deformation and thereby the larger deviation. In addition, as Fig. 4(d) shows, the time shift can be well eliminated by modifying the deformation effect.

Then we move our focus to the long trajectory HHG. As Fig. 5(a) shows, the emission time shift Δt_r of long trajectory harmonics is obviously smaller than short ones. It can be explained by two aspects. One reason is that the long trajectory electrons drift further from the parent ion and thereby feel weaker than the Coulomb potential. As Fig. 5(b) shows, the degree of deformation is smaller than that in Fig. 3(f). The other reason is attributed to the chirp of HHG. As Fig. 2(c) illustrates, the deformation makes the electron recollide with the core earlier and with higher kinetic energy. Therefore the Ω-t_r curve shifts both left (smaller t_r) and upward (higher Ω). For short trajectory harmonics with positive chirp, both these two kinds of shift contribute to positive Δt_r, while for long
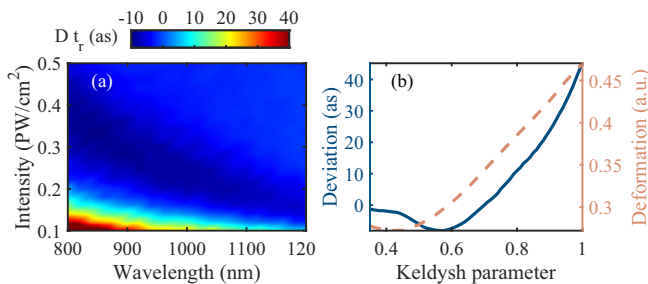

FIG. 5. (a) The emission time shift of the QO model for long trajectory HHG. (b) The average time shift and degree of deformation.

trajectory harmonics with negative chirp these two kinds of shift have opposite effect, which reduces the total deviation and even makes Δt_r negative.

Here we can delve into a discussion about the origin of the time shift. The Coulomb effect can be decomposed into short-range and long-range effect. The classical model fails to account for both the short-range and long-range effect, thus exhibiting the most obvious deviation. The QO model is accurate in the limit of short-range potential [32]. The short-range effect mainly influences the ionization. It makes electrons spend so-called tunneling time to pass through the barrier. The tunneling time and nonzero tunnel exit are important for ionization and return time [25,54]. The QO model ignores the long-range Coulomb interaction after ionization. The long-range Coulomb effect has more intricate influence. It can be seen as an influence on parabolic free electron dispersion. The influence consists of low-order dispersion and high-order dispersion. In the parameter region $\gamma \ll 1$, the high-order effect is weak, and thereby the SPA is still effective. Previous Coulomb-corrected models based on SPA are valid. In contrast, we demonstrate that in the parameter region $\gamma \approx 1$ the high-order dispersion becomes non-negligible. The group delay dispersion and higher-order dispersion lead to the electron wave-packet deformation. In this case, the modifications within the framework of SPA are no longer appropriate.

The above results reveal the important influence of wave-packet deformation on emission time. Though the absolute emission time is difficult to measure directly, the influence of wave-packet deformation can be revealed in observables of two-color field experiments [18,20,55].

We first consider the interferometry experiment formed by adding a perturbative second harmonic (SH) field in the parallel direction of the fundamental laser [19,34]. The SH pulse perturbs electron trajectories differently in the adjacent half cycle. Thus the dynamical symmetry is broken, which leads to the generation of even order harmonics. As the SH field is much weaker than the fundamental field, the electron trajectories remain unchanged but an additional phase ς is introduced with opposite sign in the adjacent half cycle. The intensity of even harmonics is modulated with phase delay ϕ between two lasers:

$$\varsigma(\Omega, \phi) = \int_{t_i}^{t_r} [\mathbf{v}(\tau)\mathbf{A}_2(\tau, \phi)]d\tau,$$

$$I(\Omega, \phi) \propto \sin^2[\varsigma(\Omega, \phi)]. \tag{17}$$

Here $\mathbf{A}_2$ is the vector potential of the SH field. In TDSE simulation, not only the subcycle interference but also the ground-state depletion and pulse envelope can influence the modulation. Moreover, the multirecombination trajectory harmonics can also disturb the results. In order to prevent the above influences, we calculate $I(\Omega, \phi)$ as

$$I(\Omega, \phi) = |\mathbf{E}_G(\Omega, t_r, \phi) - \mathbf{E}'_G(\Omega, t'_r, \phi + \pi)e^{-i\Omega(t'_r - t_r)}|^2. \tag{18}$$

The $\mathbf{E}_G$ and $\mathbf{E}'_G$ represent the Gabor distribution when the phase delay is ϕ and $\phi + \pi$, respectively. The trapezoidal envelope has one-cycle rising and falling edges and a one-cycle plateau. t_r and t'_r are the temporal locations of maxima that lie between 1.2 and 1.7 o.c.
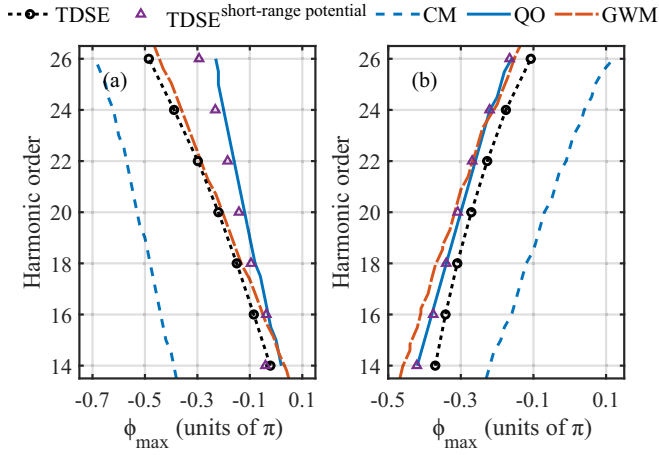
FIG. 6. The optimal phase delay that makes even order harmonics maximal. (a) The results of short trajectory HHG. (b) The results of long trajectory HHG. The intensity of the fundamental field is 0.15 PW/cm^2 and the wavelength is 800 nm. The intensity of the SH field is 0.1% of the fundamental field.

We first focus on the results of short trajectory HHG shown in Fig. 6(a). Here ϕ_{max} is defined as the optimal phase delay that makes the intensity of even harmonics maximal. The intensity of the fundamental field is 0.15 PW/cm^2 and the wavelength is 800 nm. The intensity of the SH field is 0.1% of the fundamental field. The black circles and dashed line denote the TDSE result. With harmonic order increasing from 14 to 26, ϕ_{max} changes from 0 to -0.5π. The CM result shown by the blue dashed line exhibits obvious disagreement with the TDSE result. The deviation goes as high as 0.3π. The QO result shown by the blue solid line also exhibits notable deviation. Its average deviation is about 0.12π. Additionally, the deviation increases with harmonic order and reaches 0.25π near the cutoff. The above deviation is non-negligible for application of HHS [16] and other investigations such as terahertz wave generation [56,57]. The purple triangles display the short-range potential TDSE result. It is consistent with the QO result, meaning the deviation mainly stems from long-range Coulomb effect. The orange line shows the GWM result. We use the effective trajectory to modify the QO trajectory after t_m. In fact, the Coulomb effect on ionization time is also important [26] and can influence the $\varsigma(\Omega, \phi)$ according to Eq. (17). But for the sake of simplicity, we do not discuss the ionization process in this paper, thereby the trajectory before t_m remains unchanged. The modified GWM result is close to the TDSE result. Its average deviation is just 0.02π. Next, we move our focus to the results of long trajectory HHG shown in Fig. 6(b). In the TDSE result, ϕ_{max} changes from -0.4π to -0.1π with harmonic order increasing from 14 to 26. The CM result has obvious deviation of 0.2π. The discrepancy between QO and TDSE is smaller than that in Fig. 6(a). The average deviation of QO is about 0.04π. It corresponds to the above discussion that long trajectory harmonics have smaller time shifts. As a result, the long trajectory harmonics are preferable for the calibration of phase delay.

Next, we investigate the observables in orthogonal two-color (OTC) fields. As shown in Fig. 7(a), in OTC fields, electrons can recollide with the parent ion with nonzero
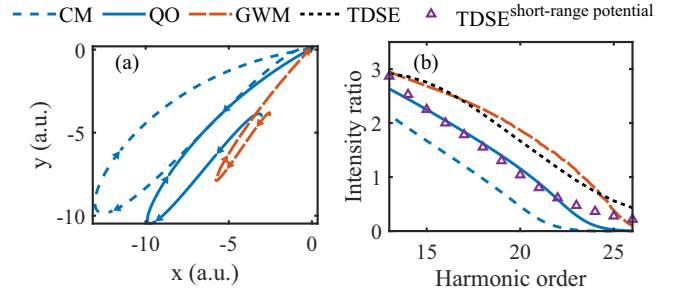

FIG. 7. (a) The trajectories of H23 from different models. (b) The intensity ratio of adjacent even and odd harmonics. The fundamental field has a wavelength of 800 nm and an intensity of 0.15 PW/cm^2. The intensity of the SH field is the same as that of the fundamental field, and the relative phase is $\pi/2$.

angles. Here the intensity of the fundamental field is 0.15 PW/cm^2 and the wavelength is 800 nm. The intensity of the SH field is the same as that of the fundamental field, and the relative phase is $\pi/2$. The trajectories in Fig. 7(a) correspond to the 23rd-order harmonics. In the GWM result, the trajectory after t_m is modified by effective trajectory. It shows that the CM result gives the smallest recollision angle, QO gives the second, and GWM gives the largest. The calibration of recollision angle is important for HHS such as orbital tomography [9,58]. Additionally, the recollision angle corresponds to the intensity ratio of adjacent even and odd harmonics [59]. As Fig. 7(b) shows, both CM and QO predict a smaller intensity ratio than TDSE results. Once again, the QO result is consistent with the short-range potential result. The GWM result corresponds well with the TDSE result. It is demonstrated that the wave-packet deformation induces not only the time shift but also the return angle shift.

According to the temporal interferometry [60], elliptically or circularly polarized HHG can be obtained by using nearly OTC fields, i.e., the crossing angle is close to $90°$:

$$D_{\pm}(\Omega) = C\{1 + \eta \exp[i(\Delta S - \Omega \Delta t_r \pm \Delta \theta_r)]\},$$

$$\zeta = \frac{|D_+|^2 - |D_-|^2}{|D_+|^2 + |D_-|^2},$$

$$\varepsilon = \mathrm{sgn}(\zeta)\left(\frac{1 - \sqrt{1 - \zeta^2}}{1 + \sqrt{1 - \zeta^2}}\right)^{1/2}. \quad (19)$$

Here $D_{\pm}$ represents the projection of high-order harmonics $\mathbf{D}(\Omega)$ onto the circular vector $\hat{\mathbf{e}}_{\pm} = (\hat{\mathbf{e}}_x \pm i\hat{\mathbf{e}}_y)/\sqrt{2}$. ζ denotes the degree of circular polarization, and ε is the ellipticity of harmonics. The sign of ε denotes the helicity. C represents the absolute amplitude of temporal emission and η is the relative amplitude ratio. ΔS, Δt_r, and $\Delta \theta_r$ denote the difference in dynamical phase S, recollision time t_r, and angle θ_r between two electron trajectories in adjacent half cycles. Note that in the following discussion the symbol Δ does not denote the deviation of the QO model. Equation (19) demonstrates that not only the time shift but also the return angle shift can influence the ellipticity. Like Young's two-slit interferometer, the distribution of the interferogram is mainly determined by the phase term $\Delta S - \Omega \Delta t_r \pm \Delta \theta_r$, and η just affects the depth of modulation. It is seen that in the first equation in Eq. (19) the only difference between D_+ and D_- is the opposite sign
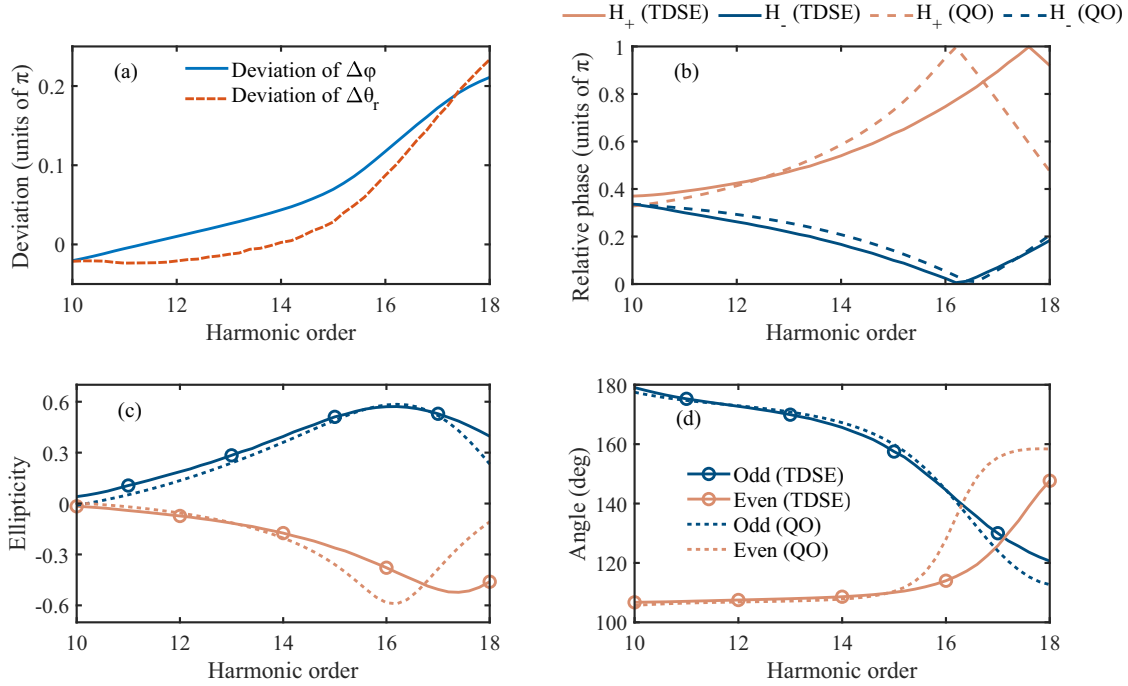
FIG. 8. (a) The deviation of the QO model. (b) The total relative phase term that determines the interferogram. (c), (d) The ellipticity (c) and the angle of the major axis (d) of each harmonic. The fundamental field has a wavelength of 800 nm and an intensity of 0.1 PW/cm². The intensity of the SH field is the same as that of the fundamental field. The phase delay is $\pi/2$, and the crossing angle is $75°$.

of $\Delta\theta_r$. For convenience, we divide the total phase term into two parts: the same term $\Delta\varphi = \Delta S - \Omega\Delta t_r$ and the opposite term $\Delta\theta_r$. First, we investigate the deviation of $\Delta\theta_r$ and $\Delta\varphi$ in the QO model. In referential TDSE calculation, θ_r and φ are extracted from Gabor analysis as

$$\theta_r = \arctan[\sqrt{I_{G_y}(\Omega, t_r)/I_{G_x}(\Omega, t_r)}],$$

$$\varphi = \arg[E_{G_\parallel}(\Omega, t_r)]. \tag{20}$$

$E_{G_\parallel}$ is the projection of Gabor distribution $\mathbf{E}_G$ onto the vector $\hat{\mathbf{e}}_\parallel = \cos\theta_r\hat{\mathbf{e}}_x + \sin\theta_r\hat{\mathbf{e}}_y$. As shown in Fig. 8(a), in the QO model both the deviation of $\Delta\theta_r$ and $\Delta\varphi$ increase with harmonic order and reach 0.2π near the cutoff. As shown in Fig. 8(b), the deviation has non-negligible influence on the total phase term. For clarity, only the even order results are shown in Fig. 8(b). The results of odd harmonics can be easily obtained via shifting by π and are not shown here. We first focus on the D_+ results shown by orange lines. In the TDSE result, the total phase $\Delta\varphi + \Delta\theta_r$ reaches π near H18, while in the QO result the peak shifts to H16. Then we focus on the D_- results shown by blue lines. Since the deviations of $\Delta\theta_r$ and $\Delta\varphi$ offset each other, the disagreement between QO and TDSE is smaller for D_-. According to Eq. (19), when $(\Delta\varphi \pm \Delta\theta_r) = (2N + 1)\pi$ and N is an integer, D_+ or D_- interferes destructively and D_- or D_+ dominates, which yields a local maxima of $|\varepsilon|$. As shown in Fig. 8(b), for even order harmonics, the destructive interference mainly occurs in D_+. Therefore the even order harmonics have negative ellipticity. Instead, the odd harmonics have positive ellipticity. As shown in Figs. 8(c) and 8(d), since the QO model has more deviation in the interferogram of D_+, it shows obvious deviation in the polarization of even harmonics.

IV. CONCLUSION

In conclusion, we have investigated the origin of emission time shift and discussed the validity of SPA in gas HHG. We revealed that the electron wave-packet deformation plays an important role in the emission time of high-order harmonics. In the experimental commonly used parameter region, it can result in a time shift of dozens or hundreds of attoseconds, which has non-negligible influence on HHS. We have demonstrated that the deformation effect, as an inherent wavelike phenomenon stemming from group delay dispersion and higher-order dispersion, cannot be well represented by trajectories within the framework of SPA. We have also revealed that the wave-packet deformation can bring notable shifts to observables in two-color field experiments. In parallel two-color fields, the deformation influences the intensity modulation of even order harmonics. In OTC fields, the deformation induces a shift in the return angles that determines the intensity ratio of adjacent even and odd harmonics. In nearly OTC fields, the time shift together with the angle shift lead to notable influence on harmonic polarization.

Our paper offers a wavelike perspective for studying the physics mechanisms behind the gas HHG process, and also provides guidance for the parameter selection in HHS applications.

[1] P. B. Corkum, Phys. Rev. Lett. **71**, 1994 (1993).

[2] T. Popmintchev, M.-C. Chen, D. Popmintchev, P. Arpin, S. Brown, S. Ališauskas, G. Andriukaitis, T. Balčiunas, O. D. Mücke, A. Pugzlys *et al.*, Science **336**, 1287 (2012).

[3] D. C. Yost, T. R. Schibli, J. Ye, J. L. Tate, J. Hostetter, M. B. Gaarde, and K. J. Schafer, Nat. Phys. **5**, 815 (2009).

[4] D. Rupp, N. Monserud, B. Langbehn, M. Sauppe, J. Zimmermann, Y. Ovcharenko, T. Möller, F. Frassetto, L. Poletto, A. Trabattoni *et al.*, Nat. Commun. **8**, 493 (2017).

[5] O. Kfir, P. Grychtol, E. Turgut, R. Knut, D. Zusin, D. Popmintchev, T. Popmintchev, H. Nembach, J. M. Shaw, A. Fleischer *et al.*, Nat. Photon. **9**, 99 (2015).

[6] Y. Mairesse, A. De Bohan, L. Frasinski, H. Merdji, L. Dinu, P. Monchicourt, P. Breger, M. Kovacev, R. Taïeb, B. Carré *et al.*, Science **302**, 1540 (2003).

[7] Z. Yang, W. Cao, X. Chen, J. Zhang, Y. Mo, H. Xu, K. Mi, Q. Zhang, P. Lan, and P. Lu, Opt. Lett. **45**, 567 (2020).

[8] J. Itatani, J. Levesque, D. Zeidler, H. Niikura, H. Pépin, J.-C. Kieffer, P. B. Corkum, and D. M. Villeneuve, Nature (London) **432**, 867 (2004).

[9] D. Shafir, Y. Mairesse, D. Villeneuve, P. Corkum, and N. Dudovich, Nat. Phys. **5**, 412 (2009).

[10] D. Baykusheva, M. S. Ahsan, N. Lin, and H. J. Wörner, Phys. Rev. Lett. **116**, 123001 (2016).

[11] P. Lan, M. Ruhmann, L. He, C. Zhai, F. Wang, X. Zhu, Q. Zhang, Y. Zhou, M. Li, M. Lein *et al.*, Phys. Rev. Lett. **119**, 033201 (2017).

[12] P. M. Kraus, B. Mignolet, D. Baykusheva, A. Rupenyan, L. Hornỳ, E. F. Penka, G. Grassi, O. I. Tolstikhin, J. Schneider, F. Jensen *et al.*, Science **350**, 790 (2015).

[13] L. He, S. Sun, P. Lan, Y. He, B. Wang, P. Wang, X. Zhu, L. Li, W. Cao, P. Lu *et al.*, Nat. Commun. **13**, 4595 (2022).

[14] L. He, Y. He, S. Sun, E. Goetz, A.-T. Le, X. Zhu, P. Lan, P. Lu, and C.-D. Lin, Adv. Photon. **5**, 056001 (2023).

[15] P. Peng, C. Marceau, and D. M. Villeneuve, Nat. Rev. Phys. **1**, 144 (2019).

[16] B. D. Bruner, H. Soifer, D. Shafir, V. Serbinenko, O. Smirnova, and N. Dudovich, J. Phys. B **48**, 174006 (2015).

[17] A. J. Uzan, H. Soifer, O. Pedatzur, A. Clergerie, S. Larroque, B. D. Bruner, B. Pons, M. Ivanov, O. Smirnova, and N. Dudovich, Nat. Photon. **14**, 188 (2020).

[18] D. Shafir, H. Soifer, B. D. Bruner, M. Dagan, Y. Mairesse, S. Patchkovskii, M. Y. Ivanov, O. Smirnova, and N. Dudovich, Nature (London) **485**, 343 (2012).

[19] O. Pedatzur, G. Orenstein, V. Serbinenko, H. Soifer, B. Bruner, A. Uzan, D. Brambila, A. Harvey, L. Torlina, F. Morales *et al.*, Nat. Phys. **11**, 815 (2015).

[20] N. Dudovich, O. Smirnova, J. Levesque, Y. Mairesse, M. Y. Ivanov, D. Villeneuve, and P. B. Corkum, Nat. Phys. **2**, 781 (2006).

[21] D. Wu, L. Li, Y. Zhan, T. Huang, H. Cui, J. Li, P. Lan, and P. Lu, Phys. Rev. A **105**, 063101 (2022).

[22] M. Lewenstein, P. Balcou, M. Y. Ivanov, A. L'Huillier, and P. B. Corkum, Phys. Rev. A **49**, 2117 (1994).

[23] A.-T. Le, H. Wei, C. Jin, and C. Lin, J. Phys. B **49**, 053001 (2016).

[24] P. Salières, B. Carré, L. Le Déroff, F. Grasbon, G. Paulus, H. Walther, R. Kopold, W. Becker, D. Milosevic, A. Sanpera *et al.*, Science **292**, 902 (2001).

[25] J. Zhao and M. Lein, Phys. Rev. Lett. **111**, 043901 (2013).

[26] S. Yue, S. Xue, H. Du, and M. Lein, Phys. Rev. A **105**, L041103 (2022).

[27] S. Yue, J. Liu, S. Xue, H. Du, and M. Lein, Phys. Rev. A **107**, 063102 (2023).

[28] J. Dubois, S. A. Berman, C. Chandre, and T. Uzer, Phys. Rev. A **99**, 053405 (2019).

[29] H. Soifer, P. Botheron, D. Shafir, A. Diner, O. Raz, B. D. Bruner, Y. Mairesse, B. Pons, and N. Dudovich, Phys. Rev. Lett. **105**, 143904 (2010).

[30] X. Xie, C. Chen, G. Xin, J. Liu, and Y. Chen, Opt. Express **28**, 33228 (2020).

[31] B. Wang, Y. Zhang, P. Lan, C. Zhai, M. Li, X. Zhu, J. Chen, P. Lu, and C. D. Lin, Phys. Rev. A **103**, 053119 (2021).

[32] L. Torlina and O. Smirnova, New J. Phys. **19**, 023012 (2017).

[33] S. Popruzhenko, J. Phys. B **51**, 144006 (2018).

[34] O. Kneller, D. Azoury, Y. Federman, M. Krueger, A. J. Uzan, G. Orenstein, B. D. Bruner, O. Smirnova, S. Patchkovskii, M. Ivanov *et al.*, Nat. Photon. **16**, 304 (2022).

[35] L. Li, P. Lan, X. Zhu, and P. Lu, Phys. Rev. Lett. **127**, 223201 (2021).

[36] L. Li, P. Lan, X. Zhu, and P. Lu, Rep. Prog. Phys. **86**, 116401 (2023).

[37] X. Zhu, M. Qin, Q. Zhang, W. Hong, Z. Xu, and P. Lu, Opt. Express **20**, 16275 (2012).

[38] R. Kosloff and H. Tal-Ezer, Chem. Phys. Lett. **127**, 223 (1986).

[39] M. Feit, J. Fleck, Jr., and A. Steiger, J. Comput. Phys. **47**, 412 (1982).

[40] C. C. Chirilă, I. Dreissigacker, E. V. van der Zwan, and M. Lein, Phys. Rev. A **81**, 033412 (2010).

[41] P.-C. Li, Y.-L. Sheu, H. Z. Jooya, X.-X. Zhou, and S.-I. Chu, Sci. Rep. **6**, 32763 (2016).

[42] A. Slyusareva, M. Y. Emelin, A. Emelina, and M. Y. Ryabikin, Radiophys. Quantum Electron. **66**, 52 (2023).

[43] A. Zair, M. Holler, A. Guandalini, F. Schapper, J. Biegert, L. Gallmann, U. Keller, A. S. Wyatt, A. Monmayrant, I. A. Walmsley, E. Cormier, T. Auguste, J. P. Caumes, and P. Salières, Phys. Rev. Lett. **100**, 143902 (2008).

[44] V. V. Strelkov, M. A. Khokhlova, A. A. Gonoskov, I. A. Gonoskov, and M. Y. Ryabikin, Phys. Rev. A **86**, 013404 (2012).

[45] S. Yu, B. Zhang, Y. Li, S. Yang, and Y. Chen, Phys. Rev. A **90**, 053844 (2014).

[46] A. Nayak, M. Dumergue, S. Kühn, S. Mondal, T. Csizmadia, N. Harshitha, M. Füle, M. U. Kahaly, B. Farkas, B. Major *et al.*, Phys. Rep.-Rev. Sec. Phys. Lett. **833**, 1 (2019).

[47] E. Pisanty, M. F. Ciappina, and M. Lewenstein, J. Phys. Photonics **2**, 034013 (2020).

[48] S. Yue, Y. Li, S. Xue, H. Du, and M. Lein, Phys. Rev. A **106**, 023117 (2022).

[49] M. F. Herman and E. Kluk, Chem. Phys. **91**, 27 (1984).

[50] E. V. van der Zwan and M. Lein, Phys. Rev. A **82**, 033405 (2010).

[51] B. Zhang and M. Lein, Phys. Rev. A **100**, 043401 (2019).

[52] B. Gottlieb, A. Lohr, W. Becker, and M. Kleber, Phys. Rev. A **54**, R1022(R) (1996).

[53] P. Dietrich, N. H. Burnett, M. Ivanov, and P. B. Corkum, Phys. Rev. A **50**, R3585(R) (1994).

[54] Y. Chen, Phys. Rev. A **84**, 043423 (2011).

[55] J. Dahlström, A. L'Huillier, and J. Mauritsson, J. Phys. B **44**, 095602 (2011).

[56] K.-Y. Kim, A. Taylor, J. Glownia, and G. Rodriguez, Nat. Photon. **2**, 605 (2008).

[57] D. Zhang, Z. Lü, C. Meng, X. Du, Z. Zhou, Z. Zhao, and J. Yuan, Phys. Rev. Lett. **109**, 243002 (2012).

[58] C. Zhai, X. Zhang, X. Zhu, L. He, Y. Zhang, B. Wang, Q. Zhang, P. Lan, and P. Lu, Opt. Express **26**, 2775 (2018).

[59] D. Shafir, Y. Mairesse, H. J. Wörner, K. Rupnik, D. M. Villeneuve, P. B. Corkum, and N. Dudovich, New J. Phys. **12**, 073032 (2010).

[60] S. Qiao, L. Li, X. Zhu, P. Lan, and P. Lu, Phys. Rev. A **104**, 023114 (2021).